IEEE Access
Multidisciplinary | Rapid Review | Open Access Journal

Received January 28, 2021, accepted February 8, 2021, date of publication February 12, 2021, date of current version April 2, 2021.

Digital Object Identifier 10.1109/ACCESS.2021.3059068

Study of Spatial Distribution Characteristics for Dust Raised by Vehicles in Battlefield Environments Using CFD

SHANGXIAN YANG, HUIMIN CHEN, LIJUAN GAO, BIN QI, PENGYU GUO, AND JIAHAO DENG

Science and Technology on Electromechanical Dynamic Control Laboratory, Beijing Institute of Technology, Beijing 100081, China

Corresponding author: Huimin Chen (laserchm@126.com)

This work was supported in part by the Pre-researched Equipment Project Foundation of China under Grant 61404160208, and in part by the Shared Technology for Equipment Development Foundation of China under Grant 41419070203.

ABSTRACT For a pulsed laser transmitted in the raised dust from battlefield vehicle movement, the premise of obtaining its transmission properties and anti-jamming method is to acquire the spatial distribution rules of dust mass concentration. In this study, the emission mechanism for vehicle-raised dust in the battlefield environment is analyzed, as well as various influencing factors of the dust emission velocity. A finite volume method (FVM)-based model for simulating the spatial dispersion of dust raised by a certain moving tank is built, and the effects of mass flow rate, traveling speed, wind speed and wind direction on the spatial distribution of dust mass concentration are explored in the battlefield environment. The results show that the raised dust is plume-shaped within the computational domain, and the spatial mass concentration of plume is positively correlated with the mass flow rate. Besides, it is necessary to determine the impact of tank travelling speed on the spatial mass concentration of dust based on the relationship between the travelling speed and the dust mass flow rate. Although front wind reduces the spatial mass concentration of dust plumes, the reduction rate decelerates when the wind speed exceeds 4 m/s. Crosswind leads to the deflection and decreased mass concentration of dust plumes. Under varying wind directions, the variation of crosswind component exerts a more pronounced influence on the spatial mass concentration of dust than that of the front wind component. This study provides a technical support for the further study of near-ground laser weapon system against vehicle dust interference in the battle field.

INDEX TERMS Battlefield environment, vehicle-raised dust, spatial mass concentration, finite volume method (FVM).

I. INTRODUCTION

Short-range laser detectors, as an important military gear, are widely used in various types of missiles and platforms such as the air-to-air missiles, surface/ship-to-air missiles and anti-radiation missiles. However, when attacking military vehicles like tanks and wheeled armored vehicles in battlefield environments (for the rigor of the discussion, battlefield environments mentioned in this article is limited to the unpaved ground in the wild), the laser detectors equipped with ground-attack ammunition are prone to false alarms and early explosions. This is attributed to the laser absorption and scattering caused by the dust raised from vehicle movement. Hence, it is profoundly significant to investigate the concentration distribution characteristics of raised dust from moving military vehicles, in order to grasp the laser transmission properties in dust environments and to improve the ground combat efficiency of the short-range laser detectors [1], [2].

Dust raising from vehicle movement in battlefield environments is a typical gas–solid two-phase flow problem. At present, the research methods of this type of problem are mainly divided into two types: actual measurement method and simulation method. Among them, the actual measurement method requires expensive experimental facilities and a large number of experiments, while the simulation method is to study the problem by establishing a model of the actual system, with low cost and obvious advantages. Gas-solid two-phase flow models include box model, Gaussian model,

The associate editor coordinating the review of this manuscript and approving it for publication was Juan Wang.

and computational fluid dynamics (CFD) model. The box model assumes that air and solid particles are uniformly distributed in the box. This distribution model is relatively simple and cannot describe the details of the particle concentration distribution [3]. The Gaussian model is the most commonly used model in the study of atmospheric dispersion. Generally, the dispersion of particles in the atmosphere is described in the far field, while the accuracy of the description of locations close to the dust source is relatively limited [4]. With the advancement of computer technology, computational fluid dynamics (CFD) has burgeoned into an emerging discipline, which has become the most common solution to the gas–solid two-phase flow problems such as dust dispersion. Capable of displaying the computational results directly, the present research methodology allows a detailed analysis of dust spatial distribution for researchers [5], [6].To date, the spatial distribution patterns for mass concentration of dust raised by battlefield vehicle movement have scarcely been discussed in the open literature, while similar studies have focused on the discrete particle dispersion in terms of the dust from vehicle traffic, vehicle exhaust emissions and tunnel dust settlement. In general, researchers have taken the pollution control perspective in investigating the spatial dispersion and sedimentation processes of $PM_{2.5}$, PM_{10} and other solid particles, who have proposed measures for reducing the ambient dust concentration accordingly.

By creating a near-field model of dust raised by vehicles on unpaved roads, Tong *et al.* [7] described the dispersion of raised dust based on the Lagrangian method, and verified the validity of the model through field tests. After dividing the dust behavior into three stages, Chen *et al.* [8] built a simplified particles system model for each stage. They simulated the vehicle-raised dust dispersion on unpaved roads in real time through a combination of particles system, CFD and behavioral simulation techniques. Although the aforementioned rare CFD-based simulation studies analyzed the dust raised by vehicles on unpaved roads, they only gave a limited presentation of data on dust concentration distribution, and failed to analyze the spatial distribution trends of dust.

Kim *et al.* [9] delved into the discrete particle formation in the turbulent exhaust plumes of diesel vehicles by using the Fluent software. Through particle track modeling and species transport modeling in the Fluent, Thiruvengadam *et al.* [10] performed 3D simulation regarding the emission of discrete particles in the exhaust pipe of an underground mine dump truck, as well as their subsequent distribution within the isolation zone. The problem is that the motor vehicle exhaust differs in emission mechanism from the dust raised by battlefield vehicles, which features smaller particle size and lower mass concentration.

Based on the theory of gas–solid two-phase flow, Zhang *et al.* [11] numerically simulated the dust mass concentration in the belt conveyor roadway with the CFD discrete phase model, and proposed regular water sprinkling of walls for addressing the dust issue. Using CFD technology combined with field measurement, Nie *et al.* [12] investigated the dust removal effects in TBM (Tactical Ballistic Missile) tunnels at varying dust removal flows, in order to achieve dust control within such tunnels. A CFD-DPM study by Zhang *et al.* [13] explored the airflow and dust pollution behaviors in the coal mine tunnels at different wind speeds. Through integration of CFD-based simulation with atomization experiment, Yu *et al.* [14] analyzed the migration and distribution of cutting dust and multi-stage atomization field by airflow effect at the 2307 fully mechanized mining face of Tangkou Coal Mine. Accordingly, they proposed a dust reduction measure consisting of multi-stage atomizing dedusting fans at the coal cutter exterior. In the above studies, the dust dispersion processes in confined spaces were analyzed primarily, where various tunnels hindered the dust dispersion. This differs distinctly from the dispersion of raised dust from battlefield vehicles in free spaces. Additionally, none of the above studies focused on analyzing effects of different environmental factors on dust distribution.

The remainder of the paper is structured as follows: To obtain the spatial distribution characteristics for mass concentration of vehicle-raised dust under different environmental factors, section 2 analyzes the mechanism of dust emission and various factors affecting the speed of dust emission. Then in section 3, a CFD-based simulation model for dust raised by a certain moving tank is created in the battlefield context. In section 4, the dispersion process of the tank-raised dust is simulated using the Fluent software, thereby analyzing the effects of mass flow rate, tank travelling speed, wind speed and wind direction on the spatial distribution of dust thoroughly. Finally, conclusions and plans for future research directions are provided in section 5.

II. DUST EMISSION MECHANISM AND RELEVANT INFLUENCING FACTORS

Given the peculiarities of the road environment and vehicles, the emission mechanism is unique for raised dust from battlefield vehicles. In general, common road environments with dust raised by motor vehicles include the urban asphalt roads and the rural unpaved earth roads, where the road surfaces are quite solid and the vehicle types are mainly private cars, as well as light or heavy trucks. Contrastively, the road environments with dust raised by battlefield vehicles are the unpaved wild grounds (in general terms, they cannot be called the road surfaces since they have not undergone long-term compaction by vehicles), where the soil is rather loose and the major vehicle types are tracked and wheeled vehicles. The emission mechanism of vehicle-raised dust in the battlefield context will be analyzed below, as well as the factors affecting the dust emission velocity.

A. EMISSION MECHANISM

Dust raised by battlefield vehicles differs fundamentally from that raised by motor vehicles on asphalt roads in terms of the emission mechanism. The dust from asphalt road vehicles is secondary dust, which is formed by the joint action of the shear and induced airflows (caused by vehicle movement)

on the road surface and dusty tires, so that the dust particles are driven to float and subsequently migrate and move with the airflows [15]. Such dust generally has lower mass concentrations and narrower distribution ranges. The dust raised by moving vehicles in battlefield environments, in contrast, has higher mass concentrations and wider distribution ranges. Fig. 1 displays the scenes of dust raised by vehicles moving on battlefields. Except for certain differences in the soil looseness and wheel types, the emission mechanism of such dust more resembles the dust raising process of motor vehicles on unpaved roads [8], [16].

FIGURE 1. Scenes of dust raised by vehicles moving on battlefields.

For the case of tracked vehicles, the emission mechanism of raised dust from battlefield vehicles is as follows: Due to the drastic squeezing, crushing and friction between the track and the ground soil, the soil adheres to the track surface and moves with the track. The soil particles are then detached quickly from the track and dispersed in the air because of the track transmission and vibration effects, as well as the airflow effect. In Fig. 2, the emission mechanism of raised dust from battlefield vehicles is explained.

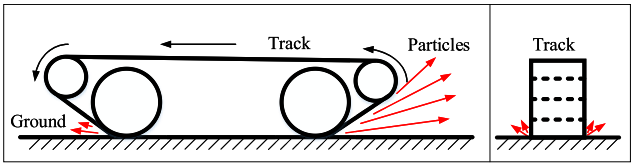

FIGURE 2. Dust emission mechanism for vehicles moving on battlefields.

In the figure, the black arrow points to the track direction and the red arrows represent the emission of dust. The ground crushing effect of track also results in slight particles jetting at the front and on both sides of the track. With the advancement of vehicle, the particles jets at the front are drawn into the track bottom, while the particle jets on both sides are ignored herein given their small dispersion ranges. Additionally, the shear and induced airflows resulting from vehicle movement still drive the dust particles on the surrounding surfaces into the air, which is though negligible in this study as well, since their concentration is considerably lower than that of the dust formed by the track crushing effect. All in all, this study only considers the dust emission concentrated at the rear track.

B. INFLUENCING FACTORS

The emission velocity of vehicle-raised dust on battlefields is associated with the ground and vehicle factors. Ground factors comprise the dust particle properties (size, density, viscosity, etc.) and the soil conditions (sand content, moisture content, etc.), whereas vehicle factors include the vehicle speed, weight, size, wheel number, track/tire tread, etc. [17], [18]. So far, a detailed analysis of such problems is unavailable in the existing literature.

In the case of road motor vehicles, the measure of vehicle-raised dust emission velocity is known as the source intensity. Currently, the source intensity of dust raised by motor vehicles is estimated often with emission factors. In the 1970s, the USEPA promulgated the Compilation of Air Pollution Emission Factors, i.e. AP-42 [19]. It provides detailed guidelines for the emissions estimation of over two hundred air pollutants including stationary sources, non-point sources, road sources and non-road sources, as well as conventional pollutants, greenhouse gases and toxic gases. In AP-42, the empirical model for the emission factor of dust raised by vehicles on unpaved roads is [7]

$$EF = \frac{k_p(s/12)^a(W/3)^b}{(M/0.2)^c}, \tag{1}$$

where EF stands for the dust emission factor (g/(km·vehicle)), k_p represents the particle size multiplier that characterizes the distribution of dust particles of different sizes (g/km), s denotes the sand content of road surface materials, i.e. the mass of silt-sized materials per unit area (g/m2), W is the mean mass of vehicles (t), and M the moisture content of road surface materials (%).

According to this model, the emission factor of dust raised by vehicles on unpaved roads is positively correlated with the particle size multiplier, sand content of road surface materials and vehicle weight, while negatively correlated with the moisture content of road surface materials. Additionally, the emission factor in the empirical model is defined as the dust emission mass during vehicle travel per unit distance, which does not involve the vehicle speed. Thus, as long as the emission factor is determined, higher vehicle speed indicates longer travel distance per unit time, and corresponding equiproportional increase in the dust emission mass. In other words, a linear relationship is present between the vehicle speed and the mass flow rate of vehicle-raised dust (dust emission mass per unit time, g/s) in the empirical model. The estimates of dust emission properties with the AP-42 model, as a purely statistical model for investigating the dust emission factors and related influencing parameters, are erroneous compared to the actual values. Nevertheless, what is certain is that the mass flow rate of raised dust from battlefield vehicles is theoretically a fixed value under constant influencing factors.

III. SIMULATION EXPERIMENTS

The simulation process of dust raised by vehicles moving on battlefields mainly comprises the creation of numerical and physical models, as well as the setting of simulation conditions. The accuracy and reliability of numerical simulations are dependent on the rationality of simulation models and the

precision of parameter settings. In the dust dispersion numerical model, both the airflow motion and the dispersion motion of dust particles should be taken into consideration. The physical model involves vehicle modeling and computational domain setting. Regarding simulation conditions, the vehicle travel information, the intrinsic properties of dust particles and the environmental factors need to be considered.

A. NUMERICAL MODELS

1) AIRFLOW NUMERICAL MODEL

The components of flow field velocity $\vec{u}$ in the x, y and z directions are denoted by u_1, u_2 and u_3, while the pressure of flow field is denoted by P. The simulation process disregards the heat transfer, and the dust dispersion follows the laws of mass and momentum conservation. The flow of dust is turbulent, and the travel of battlefield vehicles leads to high strain rate, large curvature and strong swirl flow. The turbulent motion of gas is described with the renormalization group (RNG) model. Relevant mathematical models are presented below [20], [21]

The mass conservation equation is

$$\frac{\partial \rho}{\partial t} + \frac{\partial}{\partial x_i}(\rho u_i) = S_m, \tag{2}$$

The momentum conservation equation is

$$\frac{\partial}{\partial t}(\rho u_i) + \frac{\partial}{\partial x_j}(\rho u_i u_j) = -\frac{\partial p}{\partial x_i} + \frac{\partial}{\partial x_j}\left[(\mu + \mu_t)\left[\frac{\partial u_j}{\partial x_i} + \frac{\partial u_i}{\partial x_j}\right]\right], \tag{3}$$

where $\mu_t = \rho C_\mu k^2/\varepsilon$.

The k equation is

$$\frac{\partial(\rho k)}{\partial t} + \frac{\partial(\rho k u_i)}{\partial x_i} = \frac{\partial}{\partial x_j}\left[\alpha_k \mu_t \frac{\partial k}{\partial x_j}\right] + G_k - \rho\varepsilon, \tag{4}$$

The ε equation is

$$\frac{\partial(\rho\varepsilon)}{\partial t} + \frac{\partial(\rho\varepsilon u_i)}{\partial x_i} = \frac{\partial}{\partial x_j}\left[\alpha_\varepsilon \mu_t \frac{\partial \varepsilon}{\partial x_j}\right] - R_\varepsilon + \frac{C_{1\varepsilon}\varepsilon}{k} G_k - C_{2\varepsilon}\rho\frac{\varepsilon^2}{k}, \tag{5}$$

In the above equations, ρ denotes the air density ($\mathrm{kg \cdot m^{-3}}$), k denotes the turbulent kinetic energy ($\mathrm{m^2 \cdot s^{-2}}$), ε denotes the dissipation rate ($\mathrm{m^2 \cdot s^{-3}}$), μ stands for the laminar viscosity coefficient (Pa·s), μ_t stands for the turbulent viscosity coefficient (Pa · s), and G_k is the turbulent kinetic energy derived from the mean velocity gradient ($\mathrm{kg \cdot (s^{-3} \cdot m^{-1})}$). Meanwhile, x_i and x_j ($i, j = 1, 2, 3$) are the tensor forms of turbulence model, which represent three different directions of x, y and z, α_ε and α_k are the turbulent Prandtl numbers, R_ε is the time-averaged strain rate of the fluid, and the values of $C_{1\varepsilon}$, $C_{2\varepsilon}$ and C_μ are 1.44, 1.9 and 0.09, respectively. Besides, the source term S_m represents the mass of continuously inflowing gas (kg).

2) DUST NUMERICAL MODEL

The dispersion motion of dust particles raised by moving tank is simulated with the discrete phase model (DPM) in the Fluent. As a numerical model of two-phase flow following the Euler-Lagrangian approach, DPM solves the particle motion trajectory by integrating the force differential equation of particles in the Lagrangian coordinates, which regards the fluid as a continuous phase. In the Cartesian coordinate system, the force equilibrium equation of particles is expressed as follows [22], [23]

$$\frac{\mathrm{d}\vec{u_p}}{\mathrm{d}t} = \vec{F_\mathrm{D}}(\vec{u} - \vec{u_\mathrm{p}}) + \frac{\vec{g}(\rho_\mathrm{p} - \rho)}{\rho_\mathrm{p}} + \vec{F}, \tag{6}$$

where $\mathrm{d}\vec{u_\mathrm{p}}/\mathrm{d}t$ denotes the inertial force of dust particles per unit mass, $\vec{u_\mathrm{p}}$ is the particle velocity vector (m/s), $\vec{F_\mathrm{D}}(\vec{u} - \vec{u_\mathrm{p}})$ represents the drag force function for dust particles per unit mass, $\vec{F_\mathrm{D}}$ is the drag force of dust particles per unit mass under unit speed difference (N/(m/s)), $\vec{g}(\rho_\mathrm{p} - \rho)/\rho_\mathrm{p}$ denotes the sum of gravity and buoyancy for dust particles per unit mass, ρ_p is the density of dust particles (kg/m3), and $\vec{F}$ is the additional forces on the dust particles per unit mass, which generally include the pressure-gradient force, virtual mass force, thermophoretic force, Brownian motion force, Saffman lift, Magnus lift, etc. Given the lower density of gas phase than that of dust particles in this study, the virtual mass force is zero. Meanwhile, since the heat transfer is disregarded in the dispersion process of tank-raised dust, the thermophoretic and Brownian motion forces caused by the temperature gradient are also zero.

Assuming the vehicle-raised dust is spherical particles, then the drag force conforms to the spherical drag law, which is expressed as

$$\overrightarrow{F_\mathrm{drag}} = \vec{F_\mathrm{D}}(\vec{u} - \vec{u_\mathrm{p}}) = \frac{18\mu}{\rho_\mathrm{p} d_\mathrm{p}^2}\frac{C_\mathrm{D} R_\mathrm{e}}{24}(\vec{u} - \vec{u_\mathrm{p}}), \tag{7}$$

In the above formula, C_D is the drag coefficient defined as $C_D = a_1 + a_2/R_e + a_3/R_e^2$, where a1, a2 and a3 are all constants. R_e is the Reynolds number defined as $R_e = \rho d_\mathrm{p} \left|\vec{u} - \vec{u_\mathrm{p}}\right| /\mu$, and d_p denotes the particle size (μm). Gravity and buoyancy are the two basic forces that affect the motion of dust particles. For the sake of convenience, the resultant force $\vec{F_\mathrm{f}}$ of gravity and buoyancy is expressed as follows

$$\vec{F_\mathrm{f}} = m\vec{g} - \rho\vec{g}V_\mathrm{p} = m\vec{g} - \rho\vec{g}\frac{m}{\rho_\mathrm{p}} = m\vec{g}(\rho_\mathrm{p} - \rho)/\rho_\mathrm{p} = \pi d_\mathrm{p}^3 \vec{g}(\rho_\mathrm{p} - \rho)/6, \tag{8}$$

where V_p denotes the volume of dust particles ($\mathrm{m^3}$).

Pressure gradient force $\vec{F_\mathrm{P}}$ refers to the force of differential pressure acting on dust particles in the gas phase fluid, and its expression in the x direction is

$$F_\mathrm{P} = -V_\mathrm{p}(\partial P/\partial x). \tag{9}$$

Magnus lift $\overrightarrow{F_{\mathrm{Mag}}}$ refers to the lift force generated by dust particles rotating in the gas phase, which is expressed as

$$\overrightarrow{F_{\mathrm{Mag}}} = \pi d_{\mathrm{p}}^3 \rho \vec{\omega} (\vec{u} - \vec{u_{\mathrm{p}}})/2. \tag{10}$$

When a velocity difference is present between particles and their surrounding fluid, and the velocity gradient of the fluid is perpendicular to the particle motion direction, a lift force from low to high velocities is generated due to the flow velocity difference between two sides of the particles, which is called Safman lift $\overrightarrow{F_{\mathrm{Saf}}}$. Its expression in the x direction is

$$\overrightarrow{F_{\mathrm{Saf}}} = 1.61\sqrt{\mu\rho} d_p^2 (\vec{u} - \vec{u_{\mathrm{p}}}) \sqrt{\left|\mathrm{d}\vec{u}/\mathrm{d}x\right|}. \tag{11}$$

Conclusively, the total force acting on the dust particles can be expressed as

$$\frac{\mathrm{d}\vec{u_{\mathrm{p}}}}{\mathrm{d}t} = \overrightarrow{F_{\mathrm{drag}}} + \vec{F_{\mathrm{f}}} + \vec{F_{\mathrm{P}}} + \overrightarrow{F_{\mathrm{Mag}}} + \overrightarrow{F_{\mathrm{Saf}}}. \tag{12}$$

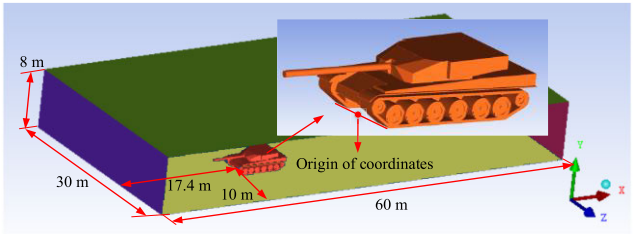

FIGURE 3. Physical model and computational domain of studied tank.

B. PHYSICAL MODEL

3D modeling of a certain tank is performed with Solidworks at a 1:1 scale, where the major contour features are highlighted and the details are simplified. Fig. 3 displays the physical model and computational domain of the tank. Disregarding the barrel, the dimensions of the tank body are 7.21 m × 3.5 m × 2.35 m. Meanwhile, setting a computational domain with appropriate size and structure is necessary, in order to study the effect of wind direction on the dust concentration distribution and to reduce the boundary perturbation. After repeated attempts and adjustments, in the end, the computational domain size is 60 m × 30 m × 8 m. There is enough distance between the tank model and the boundary of the calculation domain to ensure that the flow field is completely divergent in the simulation [24]. The center of position where the tank front track is tangential to the ground is set as the origin of coordinates, which is 17.4 m and 10 m apart from the front and left boundaries, respectively. The x-axis points towards the opposite direction of tank travel, the y-axis extends upwardly perpendicular to the ground, and the z-axis points towards the tank left side. The model built is capable of simulating the effects of various horizontal winds on the dust spatial distribution through synthesis of front wind and crosswind, which has universal applicability. Judging from the distribution range of the dust in the later text, the setting of the calculation domain is reasonable.

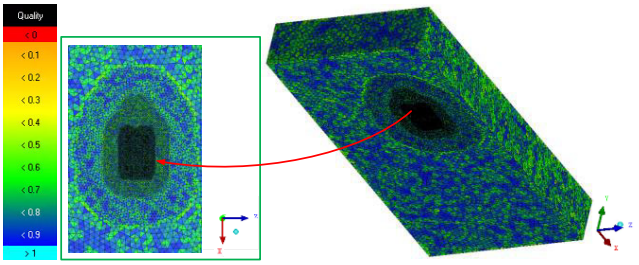

FIGURE 4. Meshing results of computational domain.

The above geometric models are meshed into tetrahedral elements using ICEM software. A high-strain-rate shear airflow is present near the tank body due to the advancement of tank. The maximal mesh size near the tank body is set as 0.1 m, the maximal mesh size far away from the tank body is set as 1 m, and the mesh growth rate is 1.1, which takes into account the computational accuracy, mesh quality and convergence rate [25], [26]. In Fig. 4, the meshing results of the computational domain are displayed. As is clear, the final mesh quantity is 2,934,078, of which elements with a quality better than 0.7 account for 89%. The percentages of mesh quality are detailed in Tab. 1. The mesh model is imported into the Fluent software for conversion into polyhedral elements and smoothing operation.

C. SIMULATION CONDITIONS

The tank traveling and track rolling processes will disturb the surrounding airflows. Conversion of motion coordinate system is required given the functional limitations of computational software. In the simulation, a relative coordinate system is established using the tank body as a reference, the tank advancement is achieved with a multiple reference frame (MRF) model, and the track rolling is simulated by setting moving walls [27], [28]. In Fig. 5, the conversion of the motion coordinate system is illustrated, where the tank travel speed is V_1, the front wind speed is V_2, and the x direction is considered the positive direction.

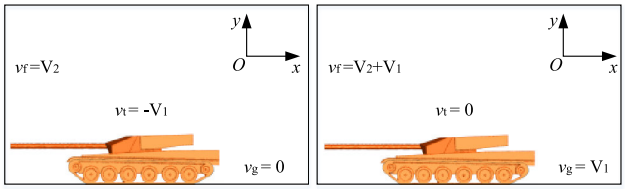

(a) Absolute coordinate system (b) Relative coordinate system

FIGURE 5. Conversion of motion coordinate system.

In the above figure, v_{f} represents the front wind speed, v_{t} represents the tank speed, and v_{g} is the ground speed. In the relative coordinate system, various track parts move at a speed of V_1 along the track rolling direction.

Size distribution of dust particles raised from tank movement is one basic characteristic parameter of discrete phase. Dust particles are grouped into a series of size bands, and their

TABLE 1. Mesh quality percentages.

Quality range	Elements	Percentage (%)
0.95 - 1.0	26674	0.909
0.9 - 0.95	2193249	74.751
0.85- 0.9	127512	4.346
0.8 - 0.85	108773	3.707
0.75 - 0.8	91721	3.126
0.7 - 0.75	78676	2.681
0.65 - 0.7	63409	2.161
0.6 - 0.65	59421	2.025
0.55 - 0.6	55047	1.876
0.5 - 0.55	57290	1.953
0.45 - 0.5	50807	1.732
0.4 - 0.45	19846	0.676
0.35 - 0.4	947	0.032
0.3 - 0.35	376	0.013
0.25 - 0.3	196	0.007
0.2 - 0.25	101	0.003
0.15 - 0.2	32	0.001
0.1 - 0.15	1	0
0.05 - 0.1	0	0
0.0 - 0.05	0	0

mass or volume percentage in each band precisely describes the particle size distribution. Test analysis is performed on the tank-raised dust collected from an experimental site by utilizing a LA-950 laser diffraction particle size analyzer (HORIBA, Japan). It is found that the minimum particle size is 1.318 μm and the maximum particle size is 262.37 μm, with a mean of 26.36 μm. Fig. 6 presents the information about size distribution of dust particles.

After least squares regression and significance testing, the dust particle sizes are found to follow the Rosin-Rammler (R-R) distribution. It is the most common function for dust particle distribution [29], [30], which is expressed as

$$F(d) = 1 - \exp\left[-\beta d^n\right], \tag{13}$$

In the above equation, $F(d)$ represents the cumulative percentage of particles less than d in size, d denotes the particle diameter, β is the characteristic parameter, and n the distribution index. Based on the data on dust particle size distribution, it is derived that $n = 1.02$, $\beta = 0.0445$.

Dust emission from tank rear is an extremely complicated motion of particle dispersion. To date, no research has been reported concerning the dust detachment ratios from various

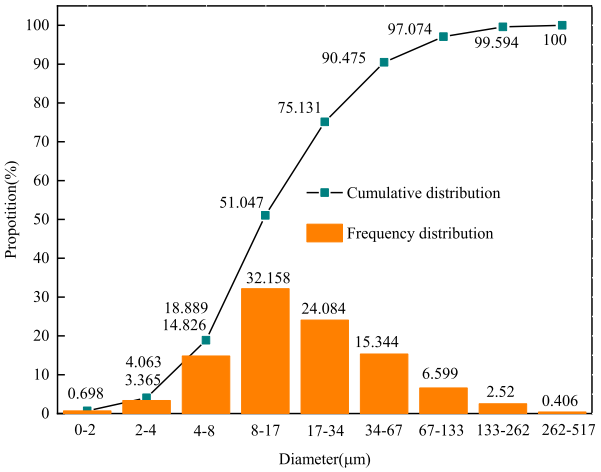

FIGURE 6. Particle size distributions of raised dust.

track parts or distribution models. The track contacts the soil sufficiently because of drastic friction. In this study, the dust particles are assumed to be detached evenly at the rear track surface. Additionally, in view of the intense and complicated turbulent motion of airflows near the tank rear, the mass of dust particles is relatively small, so that the initial velocity of dust particles becomes unimportant. In this study, the initial velocity is set to zero for all dust particles, and the solver is of transient type.

Tab. 2 lists other conditions set in the simulation.

TABLE 2. Other simulation condition settings.

Condition	Parameter	Value
Gas phase	Composition	Air
	Pressure/(Pa)	101325
Discrete phase	Bulk density/(kg/m^3)	2366
	Incident start time/(s)	0
	Incident stop time/(s)	20
Boundary	Inlet	velocity-inlet
	Outlet	pressure-outlet
	Ground	wall
	Top	symmetry
	Other sides	symmetry
	Tank surface	wall

D. MODEL VERIFICATION

In this part, the distribution of tank driving dust under basic simulation conditions is analyzed first, and then the accuracy of the simulation model is verified by combining the test data under real battlefield environment. For the case without winds, simulation analysis is performed at a tank

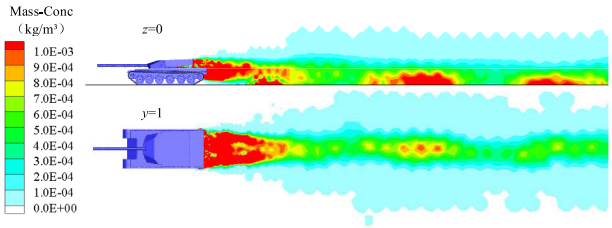

FIGURE 7. Distribution nephograms of dust mass concentration (for z = 0 m and y = 1 m cross sections).

travel speed of 45 km/h and a dust mass flow rate of 30 g/s. In Fig. 7, the nephograms of mass concentration distribution are presented during stable dust dispersion. Clearly, the dust disperses backwards from the tank rear, which is overall plume-shaped within the computational domain. The concentration of dust is highest near the rear of the tank, where the laser transmission is most disturbed.

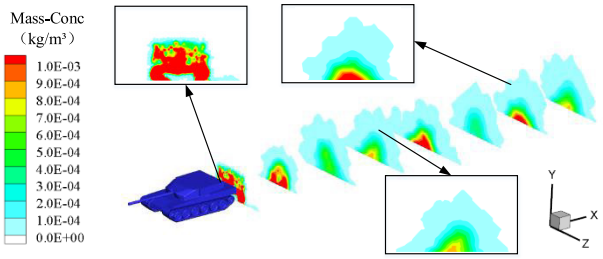

FIGURE 8. Spatial mass concentration distribution of dust plume.

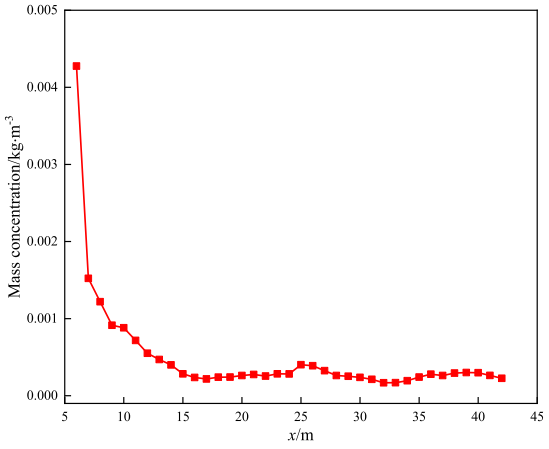

FIGURE 9. Variation trend of mean mass concentration along the x-axis.

The distribution of dust raised by moving tank is 3D. The mass concentrations of dust plumes are displayed in multiple sections along the x-axis, in order to further observation their internal structure. In Fig. 8, the spatial mass concentration distribution of dust plume is depicted. The nephogram consists of eight equally-spaced sections, which start with $x = 7$ m and end with $x = 42$ m. Obviously, the tank rear dust is concentrated primarily at the center where the plume

FIGURE 10. CEL-712 dust concentration measuring instrument.

FIGURE 11. Measurement process of the dust mass concentration.

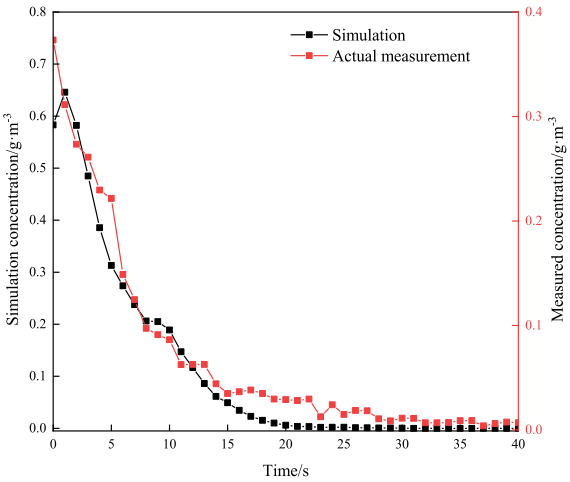

FIGURE 12. Contrast curve.

is close to the ground, and the mass concentration of the dust is reduced gradually from center outwards.

In the x direction, cross sections of dust plume are taken at 1-m intervals. For each cross section, the variation trends of mean mass concentration are obtained along the x axis, as plotted in Fig. 9. Initially, the mean mass concentrations of plume sections decrease rapidly in the x-direction, which

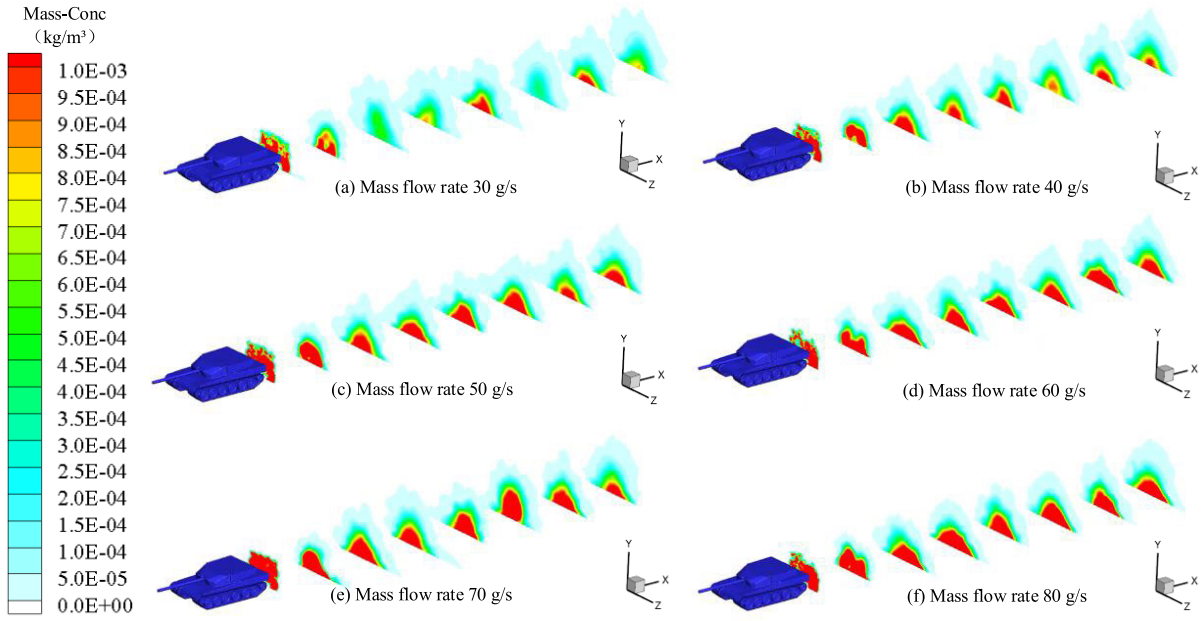

FIGURE 13. Spatial mass concentration distributions of dust plumes at various mass flow rates.

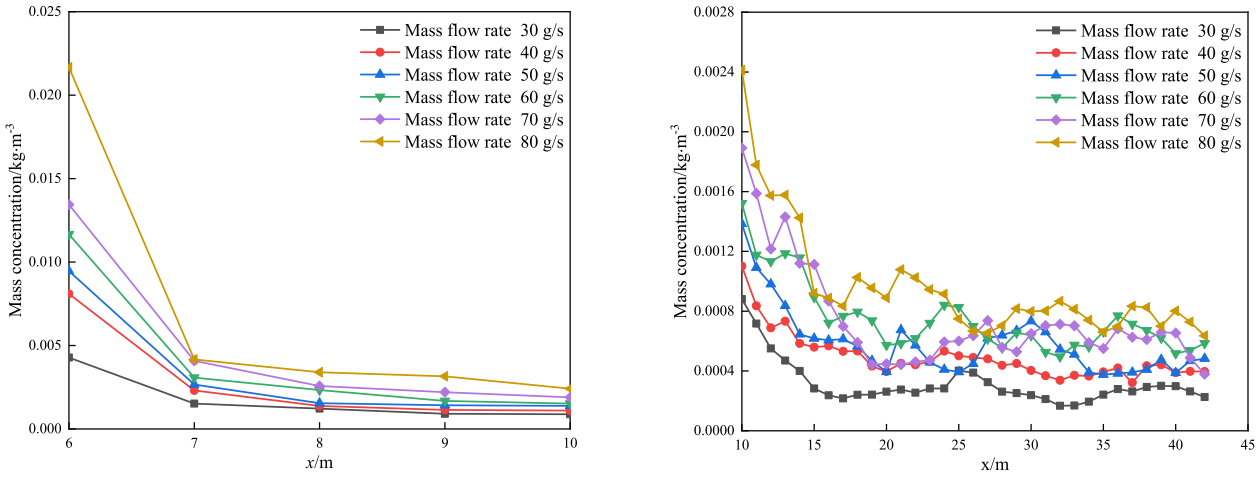

FIGURE 14. Variation trends of mean mass concentrations along the x-axis.

then fluctuate within a certain range. The reason is that the mass concentration is the highest just at dust generation at the tank rear, which then drops rapidly with the relative motion between dust and tank and the dispersion motion of dust itself. Given the complexity of turbulent motion, the mean mass concentration does not present a near-to-far monotonous decline.

From the perspective of spatial distribution, the plume distribution of the above simulation results is consistent with the distribution of the dust from the tank driving in the real battlefield environment as shown in Fig. 1. Subsequently, the variation trend of the simulated and measured dust concentration with time will be compared. On the one hand, after the dust diffusion state of the above simulation model is stable, the reference coordinate system is switched from the relative coordinate system to the absolute coordinate system, and the change of the dust mass concentration at the feature point (20 m, 1 m, 0 m) behind the tank is monitored over time. On the other hand, the CEL-712 dust concentration measuring instrument manufactured by Casella company in the UK was used to measure the dust mass concentration of tank driving in a test field. The soil of the test field is loam, and the other dust raising conditions are basically consistent with the simulation conditions.

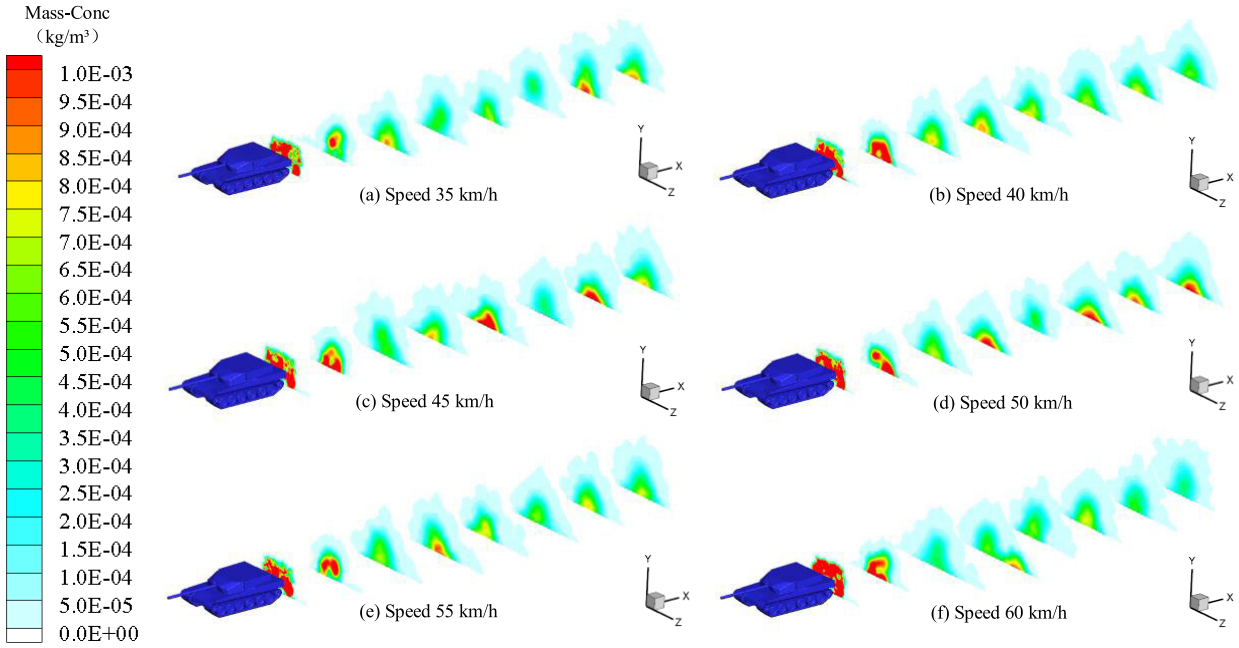

FIGURE 15. Spatial mass concentration distributions of dust plumes at various tank speeds.

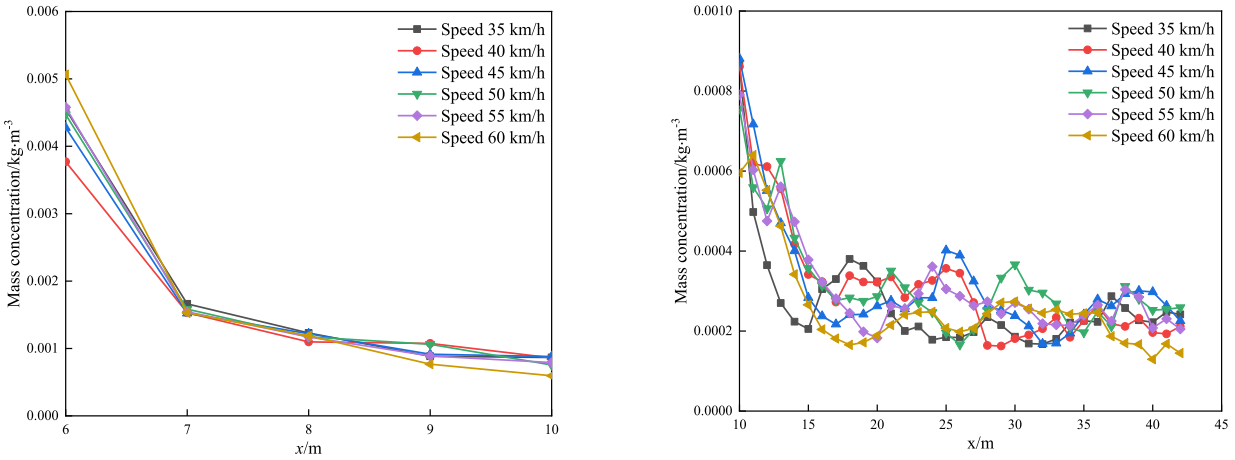

FIGURE 16. Variation trends of mean mass concentrations along the x-axis.

Fig. 10 shows the CEL-712 dust concentration measuring instrument. The instrument can realize online monitoring of the mass concentration of dust. Fig. 11 shows the measurement process of the dust mass concentration. After the tank has traveled, the dust concentration measuring instrument is penetrated into the center of the dust area through a slender rod for measurement. The height of the measuring point is 1 m.

The variation trend of the simulation and actual measurement of the dust mass concentration over time is compared and the contrast curve is plotted in Fig. 12. It can be seen that the overall trend of the two curves gradually declines with the passage of time, starting to decline rapidly, and declining slowly in the later period. The correlation coefficient of the two curves is 0.982, which is highly correlated. This indicates that the simulation model has high accuracy.

IV. SIMULATION RESULTS AND DISCUSSIONS

The spatial distribution results for mass concentration of dust from moving tank are derived under multiple influencing factors based on the Fluent software, which are categorized into scenarios with and without winds. In the scenario without winds, the effects of mass flow rate and tank speed on the dust mass concentration are analyzed primarily. In the scenario with winds, the main analytical targets are the effects of front

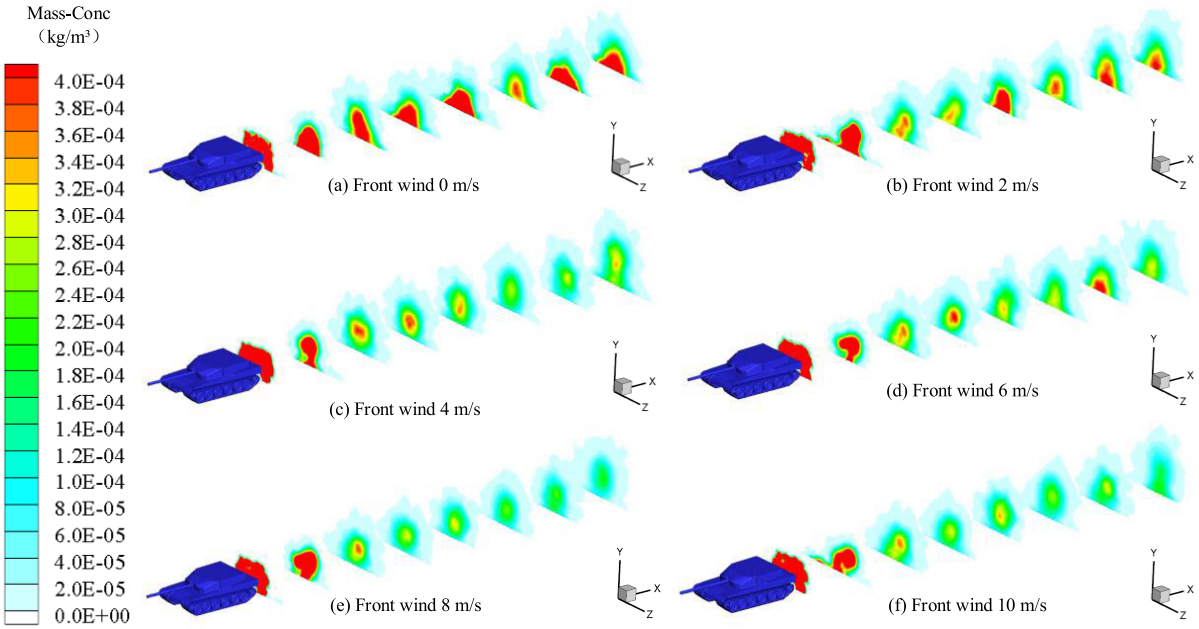

FIGURE 17. Spatial mass concentration distributions of dust plumes at various front wind speeds.

wind speed, crosswind speed and wind direction on the dust mass concentration.

A. ANALYSIS IN THE ABSENCE OF WINDS

1) DIFFERENT MASS FLOW RATES

Mass flow rate refers to the mass of dust emitted per unit time. In the foregoing section, the influencing factors for the mass flow rate of dust raised by vehicle have been analyzed. By simulating the dust raised by a tank travelling at 45 km/h, whose mass flow rates are 30, 40, 50, 60, 70 and 80 g/s, respectively, the spatial mass concentration distributions of dust plumes are obtained at different mass flow rates, as illustrated in Fig. 13. Clearly, the overall mass concentration of dust plumes increase gradually with the elevating mass flow rate.

In the following sections, the dust plumes are demarcated into a high-mass concentration segment and a low-mass concentration segment by x = 10 m, in order to observe the data variation trends clearly. The variations of mean mass concentration of dust plumes are analyzed along the x-axis under different factors. In the x direction, cross sections of dust plumes at different mass flow rates are taken at 1-m intervals. For each cross section, the variation trends of mean mass concentration are obtained along the x axis, as plotted in Fig. 14. Overall, the mass concentration values of dust plumes increase with the increasing mass flow rate in both the high- and low-mass concentration segments. Nevertheless, not all of plume sections exhibits linearly increasing mean mass concentration with the elevating mass flow rate, and this is attributed the randomness of turbulent motion.

2) DIFFERENT TRAVEL SPEEDS

To date, there has been no research relating to the influence law of tank travel speed on the mass flow rate of dust emission. In the foregoing section, the empirical model for the AP-42 dust emission factor of vehicle moving on unpaved road is analyzed, which finds a linear relationship between the dust mass flow rate and the vehicle speed under constant road conditions. In this section, the above empirical model will be utilized to compare the differences in spatial mass concentration of dust at various tank speeds. The tank speeds are set to 35, 40, 45, 50, 55 and 60 km/h, respectively. The dust mass flow rates are linear with the corresponding tank speeds except at 45 km/h, where the mass flow rate is 30 g/s. Fig. 15 depicts the spatial mass concentration distributions of dust plumes at various tank speeds. According to these nephograms, the overall mass concentrations of dust plumes present indistinct change tendencies with the increasing tank speed.

Similarly, in the x direction, cross sections of dust plumes under different tank speeds are taken at 1-m intervals. For each cross section, the variation trends of mean mass concentration are obtained along the x axis, as plotted in Fig. 16. Ignoring the turbulence effect, insignificant differences are observed in the spatial mass concentration between the dust plumes under different tank speeds from the graphs. This is attributable to the limited length of computational domain in the x-direction. In the above tank speed settings, it always takes a considerably short time for the dust particles from leaving the tank rear to escaping the computing domain, so that the radial dispersion ranges of plumes differ insignificantly. Moreover, according to the AP-42 model, the change

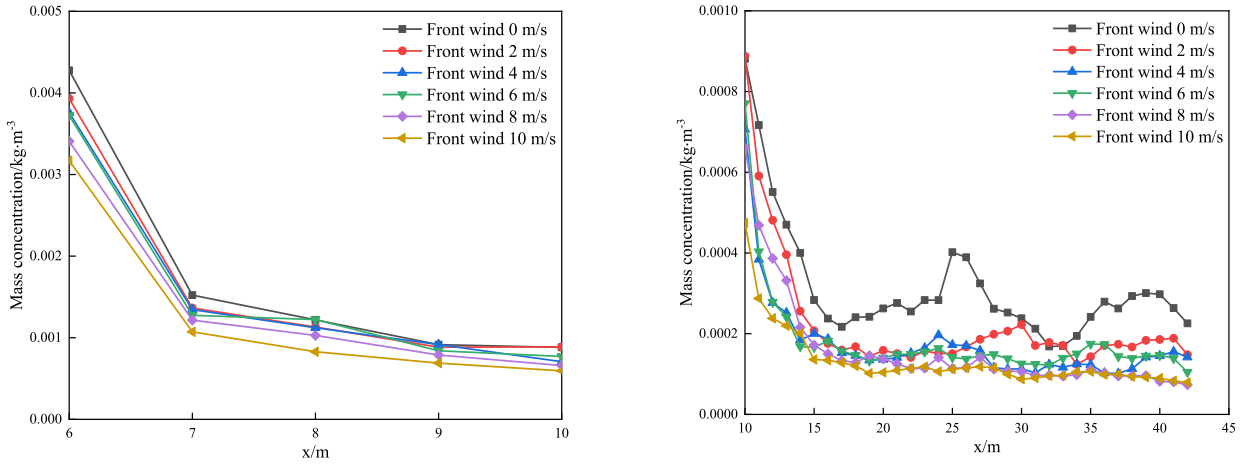

(a) High concentration segment

(b) High concentration segment

FIGURE 18. Variation trends of mean mass concentrations along the x-axis.

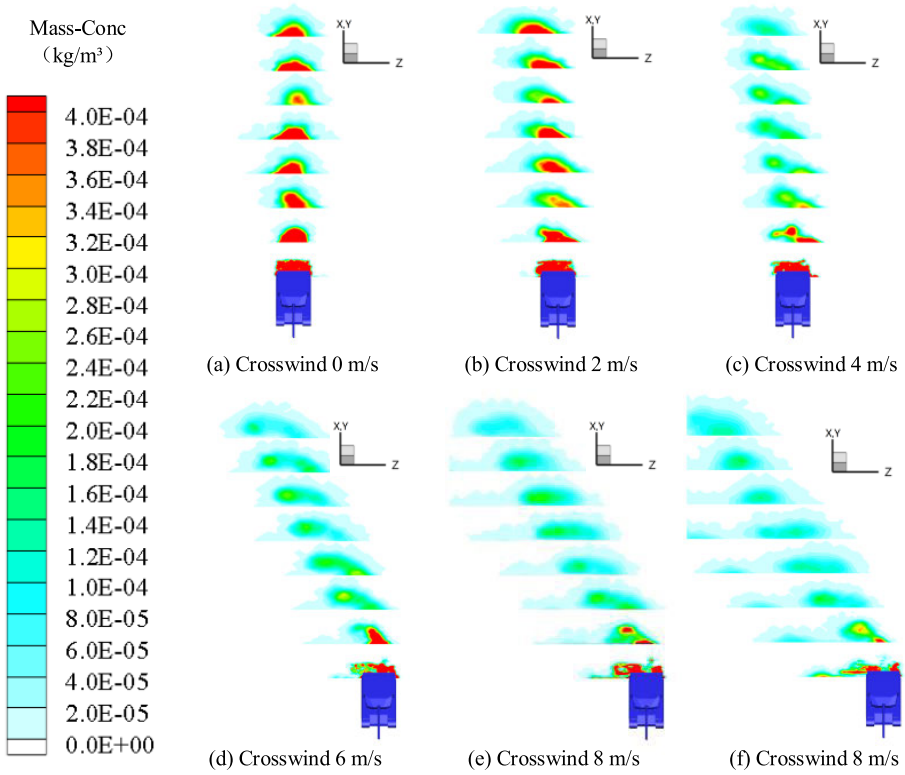

(a) Crosswind 0 m/s (b) Crosswind 2 m/s (c) Crosswind 4 m/s

(d) Crosswind 6 m/s (e) Crosswind 8 m/s (f) Crosswind 8 m/s

FIGURE 19. Spatial mass concentration distributions of dust plumes at various crosswind speeds.

in tank travel speed leads to equi-proportional changes in the axial dispersion space and mass flow rate of dust plumes. Thus, little differences are noted in the spatial mass concentrations of dust plumes corresponding to the above tank speeds.

In summary, the effect of tank speed on the spatial mass concentration of dust plume should be determined based on the relationship between travel speed and dust mass flow rate. Specifically, if the mass flow rate increases faster than the tank travel speed, the spatial mass concentration of dust plume will increase, and vice versa.

B. ANALYSIS IN THE PRESENCE OF WINDS

1) DIFFERENT FRONT WIND SPEEDS

At a tank travel speed of 45 km/h and a dust mass flow rate of 30 g/s, simulations are performed on the dust raised by moving tank separately at front wind speeds of 0, 2, 4, 6,

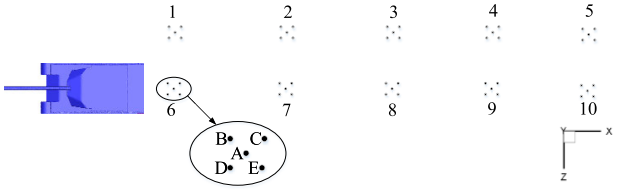

FIGURE 20. Distribution of sampling areas.

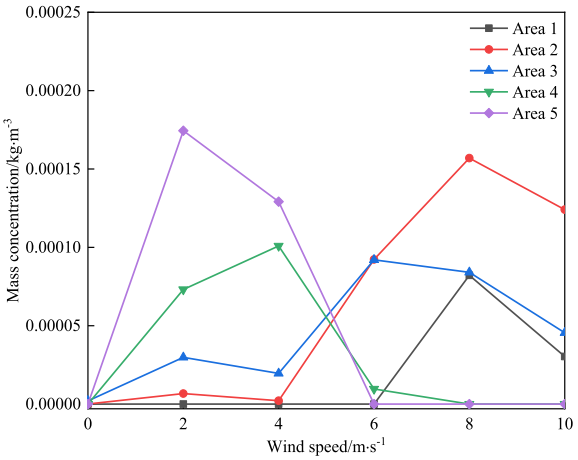

FIGURE 21. Variations of dust mass concentrations with crosswind speed in sampling areas 1-5.

8 and 10 m/s. Accordingly, the spatial mass concentration distributions of dust plumes are obtained at different front wind speeds, as illustrated in Fig. 17. Insignificant differences are noted in the plume distribution range under different front wind speeds within the computational domain. In the presence of front winds, the spatial mass concentrations of dust plumes are slightly lower than in the absence of winds.

In the x direction, cross sections of dust plumes under different front wind speeds are taken at 1-m intervals. For each cross section, the variation trends of mean mass concentration are obtained along the x axis, as plotted in Fig. 18. On the whole, the mass concentrations of dust plumes in the high concentration segment decrease gradually with the increasing front wind speed. Regarding the low concentration segment, the spatial mass concentration is the highest for the dust plume without wind disturbance, followed by the dust plume under a front wind speed of 2 m/s. Although the dust plumes at front wind speeds of 4, 6, 8 and 10 m/s have lower spatial mass concentrations, the concentration differences between them are smaller. To sum up, the spatial mass concentrations of dust plumes decrease slightly due to the accelerated dust dispersion in the x direction by the front winds. Nevertheless, such decrease slows down even with the increasing front wind speed at speeds exceeding 4 m/s.

2) DIFFERENT CROSSWIND SPEEDS

Simulations are performed on the dust raised by moving tank separately at crosswind speeds of 0, 2, 4, 6, 8 and

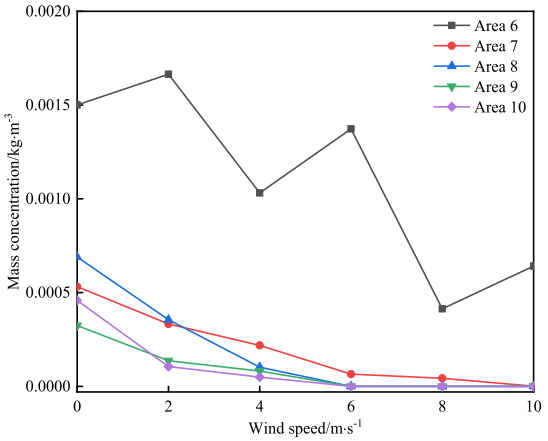

FIGURE 22. Variations of dust mass concentrations with crosswind speed in sampling areas 6-10.

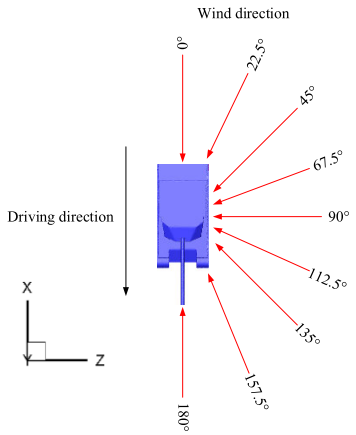

FIGURE 23. Angles of wind directions with respect to driving direction.

10 m/s under a tank travel speed of 45 km/h and a dust mass flow rate of 30 g/s. Accordingly, the spatial mass concentration distributions of dust plumes are obtained at different crosswind speeds, as illustrated in Fig. 19. It can be seen that the crosswinds cause deflection of dust plumes. As the crosswind speed increases, the plume deflection is intensified, and the dust disperses to larger ranges at lower mass concentrations.

A method for sampling the spatial mass concentrations of dust plumes is developed, in order to numerically analyze the effects of crosswind on the plume deflection and mass concentration. Fig. 20 displays the distribution of sampling areas. On the $y = 1$ m plane, points (8 m, 1 m, −4 m), (16 m, 1 m, −4 m), (24 m, 1 m, −4 m), (32 m, 1 m, −4 m), (40 m, 1 m, −4 m), (8 m, 1 m, 0 m), (16 m, 1 m, 0 m), (24 m, 1 m, 0 m), (32 m, 1 m, 0 m) and (40 m, 1 m, 0 m) are selected as the centers of areas 1, 2, 3, 4, 5, 6, 7, 8, 9 and 10. The areal concentration values are calculated by ''five-point averaging''. Taking the area 6 as an example, the points A (8 m, 1 m, 0 m), B (7.5 m, 1 m, −0.5 m), C (8.5 m, 1 m, −0.5 m), D (7.5 m, 1 m, 0.5 m) and E (8.5 m, 1 m, 0.5 m) are selected as

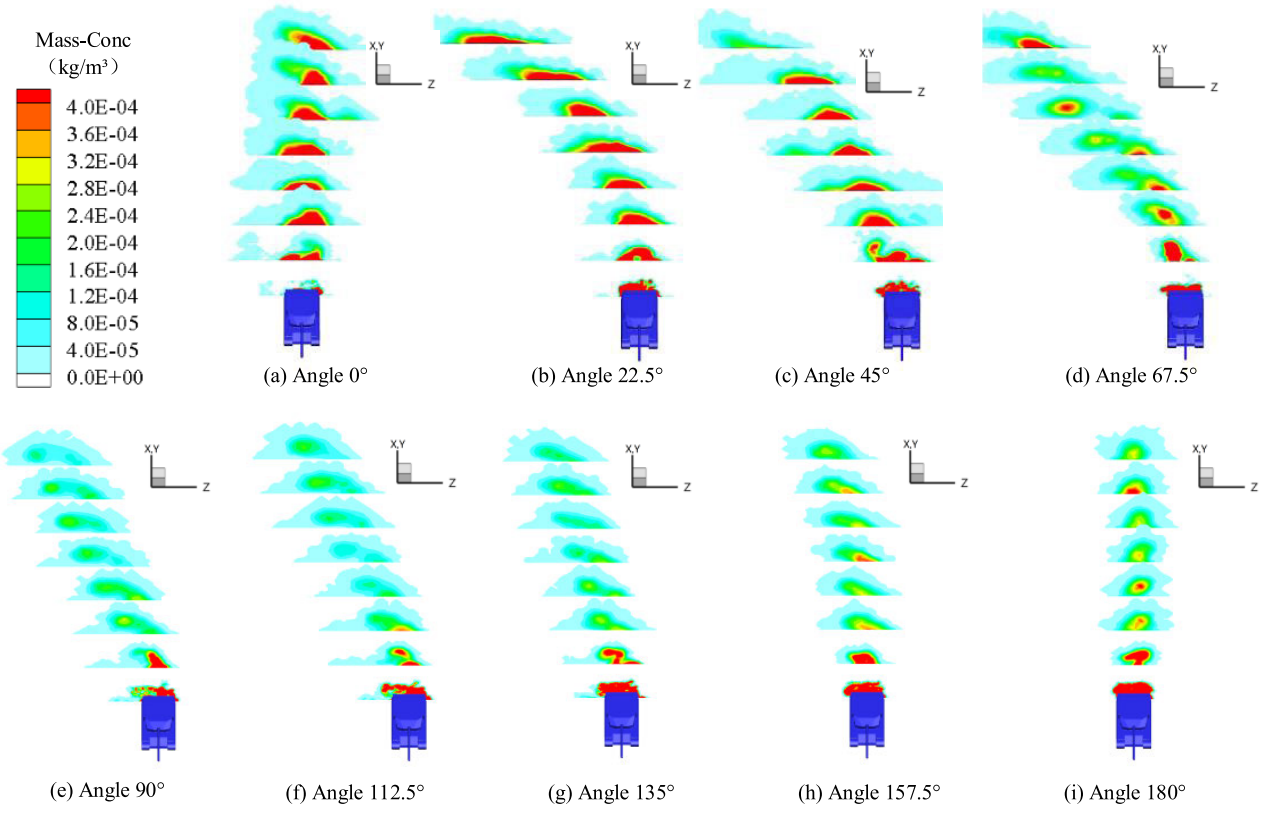

FIGURE 24. Spatial mass concentration distributions of dust plumes under various wind directions.

the sampling points, while the sampling points for other areas are similar to this area. After obtaining the concentration data of sampling points, the average concentration value of five sampling points is calculated for each area to represent the areal mean concentration. The overall variation trends of dust plumes are grasped by analyzing the concentration changes in specific sampling areas within the computational domain.

In Fig. 21, the mass concentration variations with the crosswind speed are depicted for the sampling areas 1-5. In the absence of crosswinds, the dust mass concentrations in the five sampling areas are all zero. Overall, as the crosswind speed increases, the dust mass concentrations in various sampling areas tend to increase initially and then decrease, and the peak mass concentrations have a certain sequential order. This is attributed to the relatively high mass concentration at the central axis of plume horizontal sections, so that the sampling areas 5-1 are swept by the central axis sequentially with the deflection of plumes.

For sampling areas 6-10, the variations of dust mass concentrations with the crosswind speed are depicted in Fig. 22, where the general trend is decreasing mass concentration with the increasing crosswind speed. For sampling area 6, the mass concentration fluctuates markedly with the increasing crosswind speed, since it is affected severely by the turbulence at the tank rear. The mass concentrations of areas 7-10 present a marked downward trend with the increasing crosswind speed, which decrease fundamentally to zero at wind speeds higher than 8 m/s. On the whole, deflection of dust plumes is intensified as the crosswind speed increases, thus resulting in gradually decreasing mass concentrations in the area directly behind the tank.

3) DIFFERENT WIND DIRECTIONS

At a wind speed of 6 m/s, a tank travel speed of 45 km/h and a dust mass flow rate of 30 g/s, simulations are performed on the dust raised by moving tank separately under different wind directions. The ambient winds in different directions can be decomposed into components that are parallel and perpendicular to the tank travel direction. Meteorologically, the ambient winds are divided into 16 directions at 22.5° intervals. Considering symmetry, the angles of wind directions with respect to tank driving direction are 0, 22.5, 45, 67.5, 90, 112.5, 135, 157.5 and 180° in the simulation analysis. Fig. 23 displays the included angles between different wind directions and tank driving direction (hereinafter referred to as angles).

In Fig. 24, the spatial mass concentration distributions of dust plumes are displayed in various wind directions. Clearly, certain changes are noted in both the distribution range and mass concentration of dust plumes with the changing wind direction.

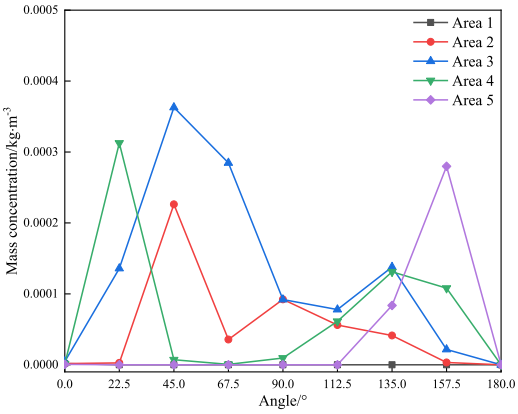

FIGURE 25. Mass concentration variations of dust with various wind directions for sampling areas 1-5.

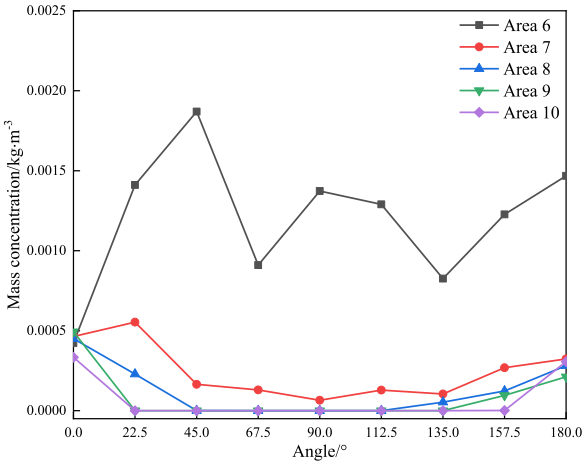

FIGURE 26. Mass concentration variations of dust with various wind directions for sampling areas 6-10.

Given the presence of crosswind component in the winds of varying directions, the dispersion range of dust plumes increases. The effects of wind direction on the plume distribution and mass concentration are analyzed by the sampling technique in Section 4.2.2. Fig. 25 plots the variations of dust mass concentrations under various wind directions for the sampling areas 1-5. As can be seen, when the angles of wind direction with respect to driving direction are 0° and 180°, the dust mass concentrations in areas 1-5 are all zero due to absence of the crosswind component. Meanwhile, in the presence of crosswind component, no dust distribution is observed in area 1 under any wind direction. For area 5, dust distribution is found only at angles larger than 112.5°, while under the remaining wind directions, no dust distribution is observed due to the substantial plume deflection at the rear area. Suggestively, in respect of dust distribution range, various wind directions produce less influence on the part of the plumes close to the dust source, while exert greater influence on the part far away from the dust source. Additionally, for areas 2, 3 and 4, the mass concentrations are overall higher when the angles are acute angles than in the case of obtuse angles. Regarding the reason, the front wind components in different wind directions lower the dust mass concentration, while the back wind components increase the mass concentration.

In Fig. 26, the mass concentration variations of dust with various wind directions are depicted for sampling areas 6-10. Due to the severe turbulence at the tank rear, the dust mass concentration presents an unmarked variation with the changing wind direction for area 6. Regarding the mass concentrations of dust in areas 7-10, they tend to decrease initially and then increase with the changing wind direction, which are distinct. This is attributed to the gradually decreasing back wind component and the gradually increasing crosswind component with the enlarging angle in the case of acute angles. Both of these changes result in lowered mass concentration of dust in the area directly behind the tank. Meanwhile, in the case of obtuse angles, the front wind component increases gradually and the crosswind component decreases gradually with the enlarging angle. Given the less impact of front wind on the mass concentration than the crosswind, the dust mass concentration increases overall in the area directly behind the tank.

V. CONCLUSION

A method for simulating dust raised by vehicles moving on battlefields is proposed based on the CFD discrete phase dispersion theory. The emission and dispersion processes of dust are simulated using the Fluent software during movement of a typical tank, thereby obtaining the influence rules of mass flow rate, tank travel speed, wind speed and wind direction on the spatial distribution characteristics of dust. The following conclusions can be drawn from the present study:

1) In the absence of winds, the raised dust is plume-shaped within the computational domain, and the highest mass concentration is found near the tank rear. The mean mass concentrations of plume sections fluctuate within a certain range following an initial rapid decrease in the x-direction. The dust plumes are clearly divisible into two parts: a high concentration segment and a low concentration segment. Turbulent motion plays a crucial role in dust raising by tank movement, which causes spatial fluctuation in the distribution of dust mass concentration.

2) At a constant tank speed, the spatial mass concentration of dust increases overall with the increasing mass flow rate. Tank travel speed affects the size of axial dispersion space of dust plumes directly, while its effect on the spatial mass concentration of dust depends on the relationship between the tank speed and the dust mass flow rate. Simulations reveal that when the tank speed is linear with the mass flow rate, the change of tank speed within a 35-60 km/h range is little influential to the plume spatial mass concentration.

3) Front wind accelerates the dust dispersion in the x-direction, although having no effect on the plume distribution range, which causes a slight decrease in the plume spatial mass concentration. As the front wind speed increases,

the reduction rate of dust mass concentration slows down at speeds higher than 4 m/s. Crosswind deflects the dust plumes, and the dust mass concentration decreases in the area directly behind the tank. At crosswind speeds exceeding 8 m/s, the dust mass concentration in the other areas directly behind the tank is basically reduced to 0, except the rear area of the tank. Under varying wind directions, the spatial mass concentration of dust plumes is influenced more pronouncedly by the crosswind component than the front wind component.

In the next step, the study of laser transmission characteristics under different dust concentration will be carried out.

REFERENCES

[1] H. Zhong, J. Zhou, Z. Du, and L. Xie, "A laboratory experimental study on laser attenuations by dust/sand storms," *J. Aerosol Sci.*, vol. 121, pp. 31–37, Jul. 2018, doi: 10.1016/j.jaerosci.2018.04.004.

[2] F. Wang, H. Chen, S. Yang, and L. Xu, "Comparison of detection performance of near-,mid-, and far-infrared laser fuzes in clouds," *Appl. Opt.*, vol. 57, pp. 8078–8086, Sep. 2018, doi: 10.1364/AO.57.008078.

[3] C. Mensink, A. Colles, L. Janssen, and J. Cornelis, "Integrated air quality modelling for the assessment of air quality in streets against the council directives," *Atmos. Environ.*, vol. 37, no. 37, pp. 5177–5184, Dec. 2003, doi: 10.1016/j.atmosenv.2003.07.014.

[4] D. J. Thomson and A. J. Manning, "Along-wind dispersion in light wind conditions," *Boundary-Layer Meteorol.*, vol. 98, no. 2, pp. 341–358, Feb. 2001, doi: 10.1023/A:1026542924429.

[5] S. Hu, Q. Liao, G. Feng, Y. Huang, H. Shao, Y. Gao, and F. Hua, "Influences of ventilation velocity on dust dispersion in coal roadways," *Powder Technol.*, vol. 360, pp. 383–694, Jan. 2020, doi: 10.1016/j.powtec.2019.09.080.

[6] W. Yin, G. Zhou, and D. Gao, "Simulation analysis and engineering application of distribution characteristics about multi-stage atomization field for cutting dust in fully mechanized mining face," *Adv. Powder Technol.*, vol. 30, no. 11, pp. 2600–2615, Nov. 2019, doi: 10.1016/j.apt.2019.08.007.

[7] X. Tong, E. A. Luke, and R. Smith, "Numerical validation of a near-field fugitive dust model for vehicles moving on unpaved surfaces," *Proc. Inst. Mech. Eng., D, J. Automobile Eng.*, vol. 228, no. 7, pp. 747–757, Jun. 2014, doi: 10.1177/0954407013512291.

[8] J. Chen, X. Fu, and E. Wegman, "Real-time simulation of dust behavior generated by a fast traveling vehicle," *ACM Trans. Model. Comput. Simul.*, vol. 9, no. 2, pp. 81–104, Apr. 1991, doi: 10.1145/333296.333366.

[9] D. Kim, M. Gautam, and D. Gera, "Parametric studies on the formation of diesel particulate matter via nucleation and coagulation modes," *J. Aerosol Sci.*, vol. 33, no. 12, pp. 1609–1621, Dec. 2002, doi: 10.1016/S0021-8502(02)00119-2.

[10] M. Thiruvengadam, Y. Zheng, and J. C. Tien, "DPM simulation in an underground entry: Comparison between particle and species models," *Int. J. Mining Sci. Technol.*, vol. 26, no. 3, pp. 487–494, May 2016, doi: 10.1016/j.ijmst.2016.02.018.

[11] F. Zhang, J. Chen, and Z. Jiang, "Numerical simulation and field measurement of dust concentration distribution in belt conveyor roadway," presented at the 2nd Int. Symp. Resour. Explor. Environ. Sci., 2018, doi: 10.1088/17551315/170-/3/032170.

[12] Q. Liu, W. Nie, Y. Hua, L. Jia, C. Li, H. Ma, C. Wei, C. Liu, W. Zhou, and H. Peng, "A study on the dust control effect of the dust extraction system in TBM construction tunnels based on CFD computer simulation technology," *Adv. Powder Technol.*, vol. 30, no. 10, pp. 2059–2075, Oct. 2019, doi: 10.1016/j.apt.2019.06.019.

[13] W. Zhang, Y. Wang, Y. Shen, Y. Wang, Y. Xu, and X. Zhang, "CFD studies of wake characteristics and power capture of wind turbines with trailing edge flaps," *IEEE Access*, vol. 8, pp. 7349–7361, Jan. 2020, doi: 10.1109/ACCESS.2020.2964620.

[14] Y. Gang, L. Dong, C. Zhenli, and Z. Zeyu, "Blended wing body thrust reverser cascade feasibility evaluation through CFD," *IEEE Access*, vol. 7, pp. 155184–155193, Nov. 2019, doi: 10.1109/access.2019.2949062.

[15] D. Sun and Y. Zhang, "Influence of avenue trees on traffic pollutant dispersion in asymmetric street canyons: Numerical modeling with empirical analysis," *Transp. Res. D, Transp. Environ.*, vol. 65, pp. 784–795, Dec. 2018, doi: 10.1016/j.trd.2017.10.014.

[16] J. Gillies, V. Etyemezian, and H. Kuhns, "Effect of vehicle characteristics on unpaved road dust emissions," *Atmos. Environ.*, vol. 39, no. 13, pp. 2341–2347, Apr. 2005, doi: 10.1016/j.atmosenv.2004.05.064.

[17] J. Veranth, E. Pardyjak, and G. Seshadri, "Vehicle-generated fugitive dust transport: Analytic models and field study," *Atmos. Environ.*, vol. 37, no. 16, pp. 2295–2303, 2003, doi: 10.1016/S1352-2310(03)00086-4.

[18] D. Williams, M. Shukla, and J. Ross, "Particulate matter emission by a vehicle running on unpaved road," *Atmos. Environ.*, vol. 42, no. 16, pp. 3899–3905, May 2008, doi: 10.1016/j.atmosenv.2008.02.003.

[19] USEPA. *AP-42: Compilation of Air Emissions Factors*. Accessed: Aug. 1, 2020. [Online]. Available: https://www.epa.gov/air-emissions-factors-and-quantification/ap-42-compilation-air-emissions-factors/

[20] S. Darmawan and H. Tanujaya, "CFD investigation of flow over a backward-facing step using an RNG k-ϵ turbulence model," *Int. J. Technol.*, vol. 10, no. 2, pp. 280–289, Apr. 2019, doi: 10.14716/ijtech.v10i2.800.

[21] G. Zhou, Q. Zhang, R. Bai, T. Fan, and G. Wang, "The diffusion behavior law of respirable dust at fully mechanized caving face in coal mine: CFD numerical simulation and engineering application," *Process Saf. Environ. Protection*, vol. 106, pp. 117–128, Feb. 2017, doi: 10.1016/j.psep.2016.12.005.

[22] R. Saman, E. Aolfazli, and E. Rahmat, "Convective heat transfer and particle motion in an obstructed duct with two side by side obstacles by means of DPM model," *Appl. Sci.*, vol. 7, no. 4, pp. 1–14, 2017, doi: 10.3390/app7040431.

[23] P. Chang, G. Xu, F. Zhou, B. Mullins, S. Abishek, and D. Chalmers, "Minimizing DPM pollution in an underground mine by optimizing auxiliary ventilation systems using CFD," *Tunnelling Underground Space Technol.*, vol. 87, pp. 112–121, May 2019, doi: 10.1016/j.tust.2019.02.014.

[24] D. Sun, X. Shi, Y. Zhang, and L. Zhang, "Spatiotemporal distribution of traffic emission based on wind tunnel experiment and computational fluid dynamics (CFD) simulation," *J. Cleaner Prod.*, vol. 282, Feb. 2021, Art. no. 124495, doi: 10.1016/j.jclepro.2020.124495.

[25] J. Thongsri, "A successful CFD-based solution to a water condensation problem in a hard disk drive factory," *IEEE Access*, vol. 5, pp. 10795–10804, Jun. 2017, doi: 10.1109/ACCESS.2017.2708138.

[26] E. Gholamalizadeh and J. D. Chung, "A parametric study of a pilot solar chimney power plant using CFD," *IEEE Access*, vol. 6, pp. 63366–63374, Oct. 2018, doi: 10.1109/ACCESS.2018.2875411.

[27] H. Patil, A. Patel, H. Pant, and V. Ananthula, "CFD simulation model for mixing tank using multiple reference frame (MRF) impeller rotation," *ISH J. Hydraulic Eng.*, pp. 2164–3040, Oct. 2018, doi: 10.1080/09715010.2018.1535921.

[28] P. Wang, N. Katopodes, and Y. Fujii, "Two-phase MRF model for wet clutch drag simulation," *SAE Int. J. Engines*, vol. 10, no. 3, pp. 1327–1337, Mar. 2017, doi: 10.4271/2017-01-1127.

[29] P. Gonzaleztello, F. Camacho, J. Vicaria, and P. Gonzalezb, "A modified Nukiyama–Tanasawa distribution function and a Rosin-Rammler model for the particle-size-distribution analysis," *Powder Technol.*, vol. 186, no. 3, pp. 278–281, Sep. 2008, doi: 10.1016/j.powtec.2007.12.011.

[30] G. Delagrammatikas and S. Tsimas, "Grinding process simulation based on Rosin-Rammler equation," *Chem. Eng. Commun.*, vol. 191, no. 10, pp. 1362–1378 Aug. 2010, doi: 10.1080/00986440490472625.

SHANGXIAN YANG was born in 1990. He received the B.S. degree and the M.S. degree in mechanical engineering from Yantai University, Yantai, in 2014 and 2017, respectively. He is currently pursuing the Ph.D. degree in weapons science and technology with the Beijing Institute of Technology, Beijing. His current research interests include transmission characteristics of laser in aerosol and distribution characteristics of vehicle dust in battlefield.

HUIMIN CHEN was born in 1973. He received the B.E. and Ph.D. degrees from the Beijing Institute of Technology (BIT), in 1998 and 2005, respectively, where he is currently pursuing the Ph.D. degree in physical electronics. He is also an Associate Professor with the Department of Armament Science and Technology, Beijing Institute of Technology. He is the youth editorial board of Infrared and Laser Engineering and Aviation Weapons. He mainly researches on short-range laser detection and information processing, laser anti-jamming, target characteristics, and other aspects of research. In the past five years, he has presided over more than ten National Natural Fund, Field Fund, Key Laboratory Fund, and Enterprise Horizontal Projects. He has published more than 40 related articles and more than 30 papers have been included by SCI and EI. He has authorized 12 invention patents, and more than 20 software copyrights. As the first author, he published Laser Fuze Technology and Short Range Laser Detection Technology.

LIJUAN GAO was born in 1987. She is currently pursuing the Ph.D. degree in mechanical engineering with the Beijing Institute of Technology, Beijing. Her current research interests include backscattering characteristics study of pulse laser and explosion dust simulation.

BIN QI was born in 1995. He is currently pursuing the M.S. degree in weapon engineering with the Beijing Institute of Technology, Beijing. His current research interest includes studying of energy type laser active interference pulsed laser fuze.

PENGYU GUO was born in 1995. He is currently pursuing the M.E. degree in weapon engineering with the Beijing Institute of Technology, Beijing. His current research interest includes backscattering characteristics study of pulse laser.

JIAHAO DENG was born in 1958. He received the M.E. and Ph.D. degrees from the Beijing Institute of Technology (BIT), in 1985 and 1998, respectively. He joined BIT, in 1985, where he is currently a Professor with the School of Mechatronical Engineering. From 2003 to 2004, he engaged in the postdoctoral research of time-frequency signal processing with the Queensland University of Technology. He is the monographer on New Magnetic Detection technology and Principles and Applications of Capacitance Detection. His main research interests include sensing, signal processing, and control technology.